Hindawi
Shock and Vibration
Volume 2022, Article ID 3896212, 17 pages
https://doi.org/10.1155/2022/3896212

Research Article

Numerical Study of Leakage and Rotordynamic Performance of Staggered Labyrinth Seals Working with Supercritical Carbon Dioxide

Hao Cao,[1] **Wanfu Zhang**,[2] **Lu Yin**,[2] **and Li Yang**[2]

[1]*State Grid Hunan Electric Power Company Limited Research Institute, State Grid Laboratory of Electric Equipment Noise and Vibration Research, Changsha, China*
[2]*School of Energy and Power Engineering, University of Shanghai for Science and Technology, Shanghai, China*

Correspondence should be addressed to Wanfu Zhang; zwf5202006@163.com

Received 20 July 2021; Revised 4 November 2021; Accepted 3 January 2022; Published 20 January 2022

Academic Editor: Giosuè Boscato

The numerical model of a staggered labyrinth seal working with supercritical carbon dioxide (S–CO_2) is established. The dynamic and static characteristics of the staggered labyrinth seal for different axial shifting distances of the rotor, various cavity geometries (heights/widths of the rotor convex plate, heights of the seal cavity), and seal clearances were investigated and compared with the conventional see-through labyrinth seal. The results show that the effective damping coefficient (C_{eff}) with positive axial shifting distance is higher than that with negative axial shifting distance. When the rotor with convex plate operates without axial shifting, the cross-coupled complex dynamic stiffness (h_R) of the staggered labyrinth seal shows little effect on the C_{eff}, and the average direct damping (C_{avg}) has a dominant influence on the C_{eff}. As the whirling frequency (Ω) is lower than 60 Hz, the C_{eff} decreases with increasing height of the rotor convex plate. For $\Omega < 140$ Hz, the damping coefficient generally increases with the decreasing height of the seal cavity. For $\Omega < 160$ Hz, the C_{eff} of the see-through labyrinth seal is about 107%–649% of the staggered labyrinth seal. Otherwise, the C_{eff} of the staggered labyrinth seal is about 105%–113% of the see-through labyrinth seal. The C_{eff} of the seal with the rotor convex plate width of 5.13 mm is relatively high, which is conducive to the stability of the system. The C_{eff} increases with the decreasing seal clearance. The C_{eff} of the seal with 0.4 mm clearance is about 116%–148% the seal with 0.6 mm. The leakage flow rate of the staggered labyrinth seal of the see-through labyrinth seal is increased by about 45.5%. The leakage flow rate of the staggered labyrinth seal decreases with the increasing convex plate height, the seal cavity height, and the decreasing seal clearance.

1. Introduction

During the 1960s–1970s, supercritical carbon dioxide (S–CO_2) was first proposed as a working fluid in a Brayton cycle by Angelino [1], Feher [2], and Combs [3]. Compared with the traditional steam cycle, S–CO_2 has many unique physical properties such as high cycle efficiency, high density, low viscosity, good performance in compression, heat transfer and stability, and nontoxic gas. It has been regarded as a promising working medium and is widely utilized for advanced turbomachines with the Brayton cycle [1, 2]. Meanwhile, the staggered labyrinth seal, which affects the leakage flow rate and system stability, is crucial for the efficient and safe operation of each turbomachine [3, 4]. For the staggered labyrinth seal working with S–CO_2, there is an urgent demand to evaluate its leakage performance and rotordynamic characteristics.

In recent years, many research institutions (Sandia National Laboratories [5], Bechtel Marine Propulsion Corporation and Bettis Atomic Power Laboratory [6, 7], Southwest Research Institute and General Electric [8–10], Tokyo Institute of Technology [11], Korea Advanced Institute of Science and Technology [12, 13], University of Central Florida [14], etc.) have carried out experimental investigations or field tests to study the performance of turbomachines including turbine expander and turbine compressor with S–CO_2. Zhang et al. [15] compared the one-dimensional design model under the three ideal gas,

compressible, and incompressible S–CO_2 physical property forms and used direct numerical simulation methods to perform three-dimensional numerical calculations. It is found that the error of the ideal gas model is up to 12%. Behafarid and Podowski [16, 17] performed aerodynamic analysis and optimized the design of the S–CO_2 turbine designed by the Korea Advanced Institute of Science and Technology and modified the turbine blades to improve the aerodynamic efficiency of the turbine components in the system. In 2016, Kim et al. [18] presented a computational fluid dynamic (CFD) analysis of a supercritical carbon dioxide, and they employed two methods of the real gas property estimations including real gas equation and real gas property (RGP) file (a required table from NIST REFPROP). The results show that the Peng–Robinson equation of estate (PREoS) method inserts a significant error in the calculation of entropy and enthalpy, while the other thermodynamic properties such as the thermal conductivity and density are almost identical to those of RGP prediction. Implementing the RGP table method indicates a very good agreement with NIST REFPROP.

For the annular seal with S–CO_2 as a working fluid, present researches mainly focus on its leakage performance. Odabaee et al. [19] proposed a turbine generator set with S–CO_2 as the working medium. The turbine part communicates with the high-speed generator through the labyrinth seal and dry gas seal to realize zero fluid leakage. In 2012, Wang et al. [20] investigated the leakage of S–CO_2 in rolling piston expander experimentally. The study compared four classic leakage models. The analysis shows that the laminar leakage model is suitable in the leakage simulation of expander. In 2013, Tian [21] performed a computational study to investigate the leakage through seals subject to large pressure differential using open-source CFD software OpenFOAM. A fluid property interpolation table program was implemented in the OpenFOAM. The results show that the carryover coefficients are independent of pressure drop across the seal and are only a function of seal geometries. In 2015, Pidaparti [22] presented a numerical study of S–CO_2 flow in see-through labyrinth seals using OpenFOAM. They also constructed a test facility and measured the leakage rate and pressure drop of S–CO_2 in the seal for various designs and conditions. The experimental and numerical results show a good agreement for a two-tooth labyrinth seal at two upstream conditions. Increasing the radial clearance and decreasing the cavity length tend to increase the leakage flow rate. There is an optimum cavity height resulting in a minimum leakage flow rate when other parameters are fixed. This trend holds true for the effect of blade quantities while holding the total length fixed. The final optimization designs and the corresponding leakage rates are different for the air and S–CO_2. In 2018, Yuan et al. [23] designed a novel test rig for traditional annular seals at the University of Virginia in the ROMAC laboratory with the goal of testing the sealing performance with S–CO_2. Bennett et al. [24] presented a numerical study of a novel stepped-staggered labyrinth seal with S–CO_2 to evaluate its performance compared with the see-through labyrinth. The computational fluid dynamic calculation was carried out using the NUMECA commercial code, and the NIST REFPROP database was used for the computation of S–CO_2 in the numerical investigation. The results show that the stepped-staggered labyrinth seals have better seal performance than the see-through labyrinth and avoid the assembly problem of axial interlocking labyrinth. The leakage flow rate increases with an increase in the radial clearance. The seal performance is worst as length/height flow rate is equal to 1, and the sealing performance shows a good symmetry of geometric topology with length/height flow rate. It may exist a best width/height flow rate that leads to the least leakage flow rate. In 2018, Zhu et al. [25] studied the design and sealing performance comparison of the 450 MWe S–CO_2 turbine shaft end seal of GE Company. In 2018, Du et al. [26] used the air and S–CO_2 model, respectively, to study the effect of working fluid on the spiral seal dry gas sealing performance under different inlet temperatures and pressures. In 2019, Du et al. [27] studied the effects of high-speed S–CO_2 dry gas seals on actual effects and analyzed the effects of actual gas effects, inertial effects, and turbulence effects on film stiffness and leakage flow rate under different medium pressure and velocity conditions. The actual gas effect makes the film stiffness and leakage flow rate increase significantly. The turbulence effect increases the film stiffness and decreases the leakage flow rate, and the inertia effect is weak.

S–CO_2 also has a potential threat to the system stability as the air and steam. Therefore, there is a pressing need to obtain the related data of the rotordynamic performance for the turbine with S–CO_2. So far, few publications or reports could be found to investigate the rotordynamic characteristics of the S–CO_2 seal. In this study, a three-dimensional numerical model of a staggered labyrinth seal working with S–CO_2 is established using the computational fluid dynamic method. An S–CO_2.rgp (real gas property) file based on the National Institute of Standard and Technology (NIST) Shen [28] was embedded in the software. A dynamic transient CFD model based on an infinitesimal theory proposed by Zhang et al. [29] was utilized to get the dynamic force coefficients for the labyrinth seal working with S–CO_2. The CFD model predicts the dynamic force coefficients for the seal operating under various rotor axial shifting distances, rotor convex plate heights/widths, seal cavity heights, and clearance conditions. The stability of the conventional labyrinth seal system was compared.

2. Numerical Method

2.1. Geometrical Model. In this study, a three-dimensional CFD numerical model of the staggered labyrinth seal, which is based on a turbine diaphragm seal, is established as the research object. Figures 1 and 2 show the two-dimensional model of the staggered labyrinth seal for this study. Table 1 gives the detailed geometric dimensions. To investigate the effect of the rotor axial shifting distance, rotor convex plate heights/widths, seal cavity heights, and clearances on the seal dynamic characteristics, the staggered labyrinth seal with five shifting distances ($z = -4$ mm, -2 mm, 0 mm, $+2$ mm, and $+5$ mm), four rotor convex plate heights ($a = 0$ mm, 1.5 mm, 2 mm, and 2.5 mm), three rotor convex plate widths

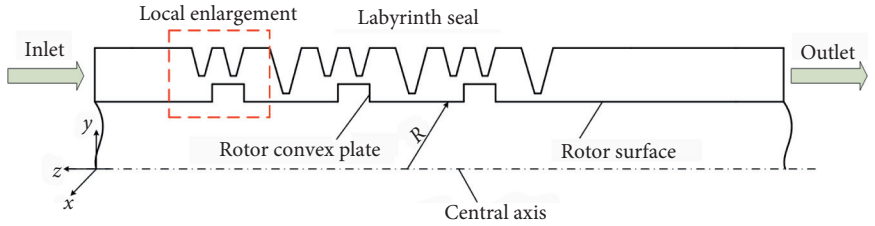

Figure 1: Two-dimensional geometry model of the staggered labyrinth seal (original model).

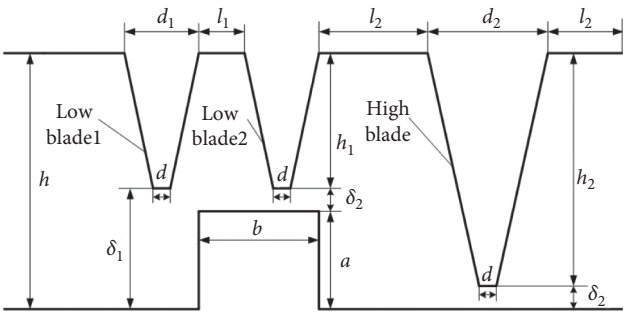

Figure 2: Local view of the staggered labyrinth seal.

Table 1: Seal dimensions.

Parameter	Value
Seal inner radius R (mm)	328.5
Cavity depth h (mm)	8.5
Low blade height h_1 (mm)	5.5
High blade height h_2 (mm)	8
Low blade root length d_1 (mm)	2.6
High blade root length d_2 (mm)	3.4
Blade thickness d (mm)	0.13
Low blade 1 and low blade 2 distance l_1 (mm)	1.4
Low blade 2 and high blade distance l_2 (mm)	3.5
High blade and low blade 1 distance l_3 (mm)	2.5
Low blade and rotor clearance δ_1 (mm)	3
High blade and rotor clearance (low blade and convex plate clearance) δ_2 (mm)	0.5
Convex plate height a (mm)	2.5
Convex plate width b (mm)	4

Table 2: Calculation conditions and parameters.

Calculation conditions	Rotor axial shifting z (mm)	Convex plate height a (mm)	Seal cavity height h (mm)	Convex plate width b (mm)	Seal clearance δ_2 (mm)	Seal type
0	0					
1	−4					
2	−2	2.5	8.5	4.00	0.5	
3	+2					
4	+5					
5		2				
6	0	1.5	8.5	4.00	0.5	Staggered labyrinth seal
7		0				
8	0	2.5	7.0	4.00	0.5	
9			5.5			
10	0	2.5	8.5	5.13	0.5	
11				6.13		
12	0	2.5	8.5	4.00	0.4	
13					0.6	
14	0	—	8.5	—	0.5	See-through labyrinth seal

($b = 4$ mm, 5.13 mm, and 6.13 mm), three seal cavity heights ($h = 5.5$ mm, 7 mm, and 8.5 mm), and three clearances ($\delta_2 = 0.4$ mm, 0.5 mm, and 0.6 mm) are employed in the numerical simulation. Table 2 gives the specific calculation conditions. In Figure 1, the rotor is shifting along the axial direction, the negative sign is shifting along the negative direction of the rotor along the z-axis, and the positive sign is shifting along the positive direction of the rotor along the z-axis.

2.2. Numerical Model. The present numerical simulation was conducted to solve the compressible RANS equations using a commercial software [29]. Table 3 lists the detailed numerical approaches for CFD analysis in this study. The working fluid is the supercritical carbon dioxide (real gas). The standard k-ε is used as the turbulence model, with the turbulence intensity of 5%. The value of $y+$ is controlled within ~300. The walls of rotor and stator are defined to be adiabatic, smooth, and have no slip. The total pressure and temperature are defined at the inlet boundary, while the average static pressure is specified at the outlet. CEL is used to define the whirling orbit of the rotor.

To improve the computational accuracy, a structured grid is employed. The blade tip, where the flow changes dramatically, is properly meshed with more grids. The scalable wall function method is used to combine the wall physical quantity with the turbulent core area. After grid independence verification, the total number of grids of the model is determined to be about 3.32×10^6 to 3.82×10^6. The detailed grid distribution is shown in Figure 3.

The ideal gas assumption is no longer applicable for the supercritical carbon dioxide. To calculate the real gas property accurately, this study generates S–CO_2.rgp (real gas property) physical property file based on NIST REFPROP [30] for CFD program call.

2.3. Rotordynamic Coefficient Solution. In this study, the seal dynamic characteristic identification method based on an infinitesimal theory is applied to solve the rotordynamic characteristics of arbitrary elliptical orbits and eccentric positions under actual conditions.

Figure 4 gives a two-dimensional schematic diagram of the rotordynamic model, assuming the rotor whirling in an elliptical orbit at any eccentric position. In the system, O is the housing center, O_1' is the rotor center, O_1 is the whirling center, and ω and Ω are the rotational speed and whirling frequency of the rotor. The new coordinate system $eO_1\alpha$ is established by taking the major and minor axis of the elliptical orbit as the coordinate axis direction, where θ is the counterclockwise rotation angle between $eO_1\alpha$ and the original coordinate system xOy. After that, the e-axis and α-axis coincide with the long and short semi-axis of the elliptical orbit, and a coordinate system (e, α) is established.

$$\begin{cases} e = m \cdot \cos(\Omega_i t), \\ \alpha = n \cdot \sin(\Omega_i t), \end{cases} \tag{1}$$

Table 3: Calculation conditions.

Parameters	Values
Fluid	S–CO_2
Turbulence model	k-ε
Wall properties	Adiabatic, smooth surface
Temperature T (K)	737
Time step/s	$1/500^* \Omega_i$
Whirling frequency Ω_i (Hz)	20, 40, ..., 240, 260
Supply pressure P_{in} (MPa)	5.7
Discharge pressure P_{out} (MPa)	5.2
Rotational speed ω (RPM)	3600
Whirling orbit	Circle orbit
Vibration amplitude	$6\%\delta_2$

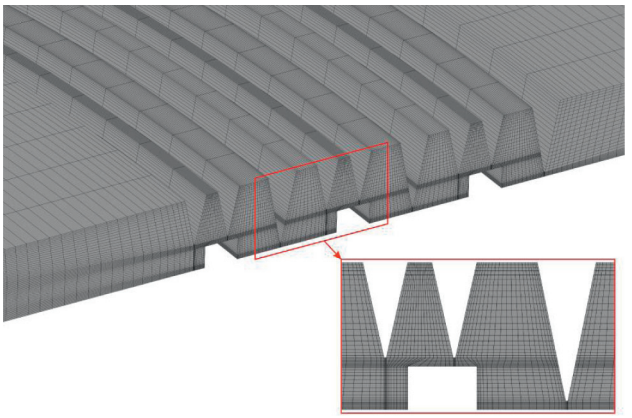

Figure 3: Grid distribution.

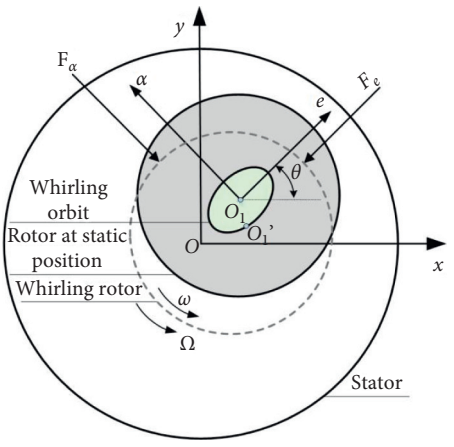

Figure 4: Rotordynamic model for annular seals.

where m and n are the length of the major and minor axis of the elliptical orbit.

In the $eO_1\alpha$, the rotor velocity is as follows:

$$\begin{cases} e = m \cdot \Omega_i \cdot \sin(\Omega_i t), \\ \alpha = n \cdot \Omega_i \cdot \cos(\Omega_i t). \end{cases} \tag{2}$$

In the $eO_1\alpha$, the rotor acceleration is as follows:

$$\begin{cases} e = m \cdot \Omega_i^2 \cdot \cos(\Omega_i t), \\ \alpha = n \cdot \Omega_i^2 \cdot \sin(\Omega_i t). \end{cases} \tag{3}$$

For a small whirling orbit of the rotor, the dynamic model can be simplified as follows:

$$\begin{aligned} -\begin{Bmatrix} \Delta F_e \\ \Delta F_\alpha \end{Bmatrix} &= \begin{bmatrix} K_{ee} & K_{e\alpha} \\ K_{\alpha e} & K_{\alpha\alpha} \end{bmatrix} \begin{Bmatrix} e \\ \alpha \end{Bmatrix} + \begin{bmatrix} C_{ee} & C_{e\alpha} \\ C_{\alpha e} & C_{\alpha\alpha} \end{bmatrix} \begin{Bmatrix} \dot{e} \\ \dot{\alpha} \end{Bmatrix} + \begin{bmatrix} M_{ee} & M_{e\alpha} \\ M_{\alpha e} & M_{\alpha\alpha} \end{bmatrix} \{\ddot{e}\ \ddot{\alpha}\}, \\ -\begin{Bmatrix} \Delta F_e \\ \Delta F_\alpha \end{Bmatrix} &= \begin{bmatrix} K_{ee} - \Omega^2 M_{ee} & K_{e\alpha} - \Omega^2 M_{e\alpha} \\ K_{\alpha e} - \Omega^2 M_{\alpha e} & K_{\alpha\alpha} - \Omega^2 M_{\alpha\alpha} \end{bmatrix} \begin{Bmatrix} e \\ \alpha \end{Bmatrix} + \begin{bmatrix} C_{ee} & C_{e\alpha} \\ C_{\alpha e} & C_{\alpha\alpha} \end{bmatrix} \begin{Bmatrix} \dot{e} \\ \dot{\alpha} \end{Bmatrix}, \end{aligned} \tag{4}$$

where $\Delta F_e = F_e - F_{e0}$, and $\Delta F_\alpha = F_\alpha - F_{\alpha 0}$. (F_e, F_α) and $(F_{e0}, F_{\alpha 0})$ are the flow-induced forces and static flow-induced forces in the e and α directions. (e, α), $(\dot{e}, \dot{\alpha})$, and $(\ddot{e}, \ddot{\alpha})$ are rotor displacements, velocities, and accelerations in the e and α directions. $(K_{ee}, K_{e\alpha}, K_{\alpha e}, K_{\alpha\alpha})$, $(C_{ee}, C_{e\alpha}, C_{\alpha e}, C_{\alpha\alpha})$, and $(M_{ee}, M_{e\alpha}, M_{\alpha e}, M_{\alpha\alpha})$ are the stiffness, damping, and mass inertia coefficients.

In the transient analysis, the seal reaction forces at $t = 0$ or $t = T/4$ in e and α directions can be stated as follows:

$$\begin{cases} \Delta F_{e\,(t=0,\Omega=\Omega_i)} = -m \cdot \left(K_{ee} - \Omega_i^2 M_{ee}\right) - n \cdot C_{e\alpha} \cdot \Omega_i, \\ \Delta F_{\alpha\,(t=0,\Omega=\Omega_i)} = -m \cdot \left(K_{\alpha e} - \Omega_i^2 M_{\alpha e}\right) - n \cdot C_{\alpha\alpha} \cdot \Omega_i, \\ \Delta F_{e\,(t=T/4,\Omega=\Omega_i)} = -n \cdot \left(K_{e\alpha} - \Omega_i^2 M_{e\alpha}\right) + m \cdot C_{ee} \cdot \Omega_i, \\ \Delta F_{\alpha\,(t=T/4,\Omega=\Omega_i)} = -n \cdot \left(K_{\alpha\alpha} - \Omega_i^2 M_{\alpha\alpha}\right) + m \cdot C_{\alpha e} \cdot \Omega_i. \end{cases} \tag{5}$$

The stiffness and damping coefficients in the coordinate system can be stated as follows:

$$\begin{aligned} \begin{bmatrix} K_{yy} - \Omega^2 M_{yy} & K_{yx} - \Omega^2 M_{yx} \\ K_{xy} - \Omega^2 M_{xy} & K_{xx} - \Omega^2 M_{xx} \end{bmatrix} &= \begin{bmatrix} \sin\theta & \cos\theta \\ \cos\theta & -\sin\theta \end{bmatrix} \begin{bmatrix} K_{ee} - \Omega^2 M_{ee} & K_{e\alpha} - \Omega^2 M_{e\alpha} \\ K_{\alpha e} - \Omega^2 M_{\alpha e} & K_{\alpha\alpha} - \Omega^2 M_{\alpha\alpha} \end{bmatrix} \begin{bmatrix} \sin\theta & \cos\theta \\ \cos\theta & -\sin\theta \end{bmatrix}, \\ \begin{bmatrix} C_{yy} & C_{yx} \\ C_{xy} & C_{xx} \end{bmatrix} &= \begin{bmatrix} \sin\theta & \cos\theta \\ \cos\theta & -\sin\theta \end{bmatrix} \begin{bmatrix} C_{ee} & C_{e\alpha} \\ C_{\alpha e} & C_{\alpha\alpha} \end{bmatrix} \begin{bmatrix} \sin\theta & \cos\theta \\ \cos\theta & -\sin\theta \end{bmatrix}. \end{aligned} \tag{6}$$

2.4. Case Verification. To verify the calculation accuracy and reliability of the present numerical method, a prior numerical simulation is carried out based on the experimental labyrinth seal model working with S–CO_2 [32]. As shown in Figure 5, the inlet pressure is set at 10 MPa, and the temperature is 45°C. The leakage flow rates of 13 different pressure ratios (0.3–0.9) were calculated and compared with the experimental results, and the calculation error is less than 8%. To verify the numerical calculation method, the experimental labyrinth seal and pocket damper seal model from Ertas et al. [19] are modeled. The results show that the numerical simulation in this study shows a pretty good prediction in the direct and cross-coupled stiffness, damping, and the effective damping of the labyrinth seal and the pocket damper seal. It verifies the reliability of the numerical method in identifying the dynamic force coefficient of the seal, as shown in Figure 6.

3. Results and Discussion

The direct complex dynamic stiffness coefficient H_R, the average direct damping coefficient C_{avg}, the cross-coupled complex dynamic stiffness coefficient h_R, and the effective damping coefficient C_{eff} are the main factors to measure the rotordynamic performance of the system. Ertas [33] experiments confirmed that $K_{xy} = -K_{yx}$. H_R, h_R, C_{avg}, and C_{eff} are defined as follows:

$$\begin{cases} H_R = \dfrac{\left[\left(K_{xx} - \Omega^2 M_{xx}\right) + \left(K_{yy} - \Omega^2 M_{yy}\right)\right]}{2}, \\ h_R = \dfrac{\left[\left(K_{xy} - \Omega^2 M_{xy}\right) + \left(-K_{yx} - \Omega^2 M_{yx}\right)\right]}{2}, \\ C_{\text{avg}} = \dfrac{\left(C_{xx} + C_{yy}\right)}{2}, \\ C_{\text{eff}} = \dfrac{C_{\text{avg}} - h_R}{\Omega}. \end{cases} \tag{7}$$

3.1. Seal Leakage. Figure 7 shows the velocity vector with a different rotor axial shifting ($z = -4$ mm, -2 mm, 0 mm, +2 mm, and +5 mm). Compared with the original model (no shifting), for $z = -2$ mm, the turbulent dissipation effect of the main vortex in the seal cavity is enhanced, and the additional small vortex effect is increased, which increases the energy dissipation and reduces the leakage. For $z = -4$ mm, the fluid through effect increases, the turbulent flow in the seal cavity is significantly reduced, the energy dissipation is insufficient, no additional small vortex is formed, and the leakage increases. For $z = +5$ mm and +2 mm, the energy dissipation in the additional small vortex is relatively small, and the leakage is relatively increased.

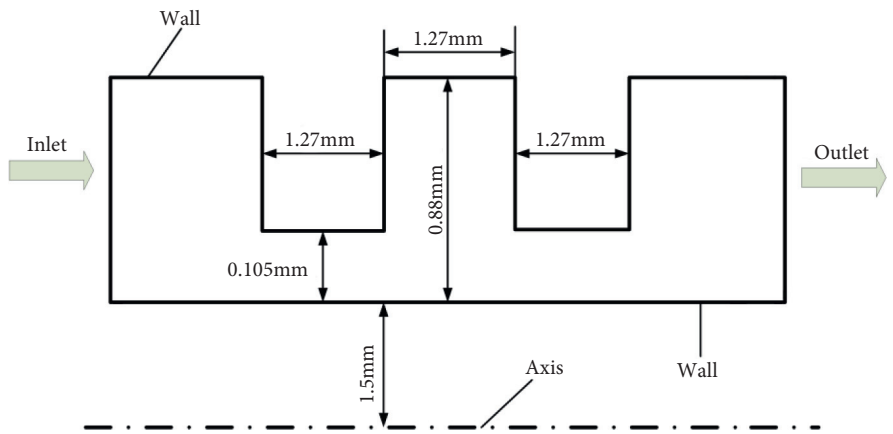

Figure 5: The experimental see-through labyrinth seal [32].

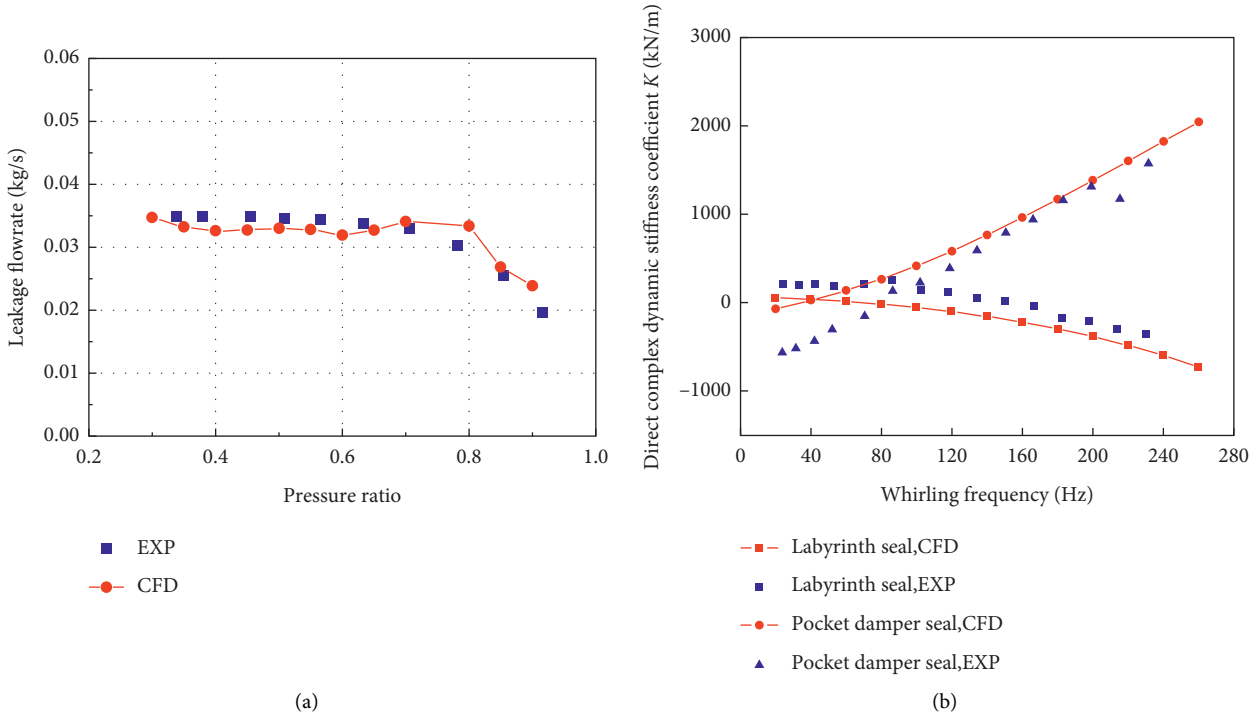

Figure 6: Continued.

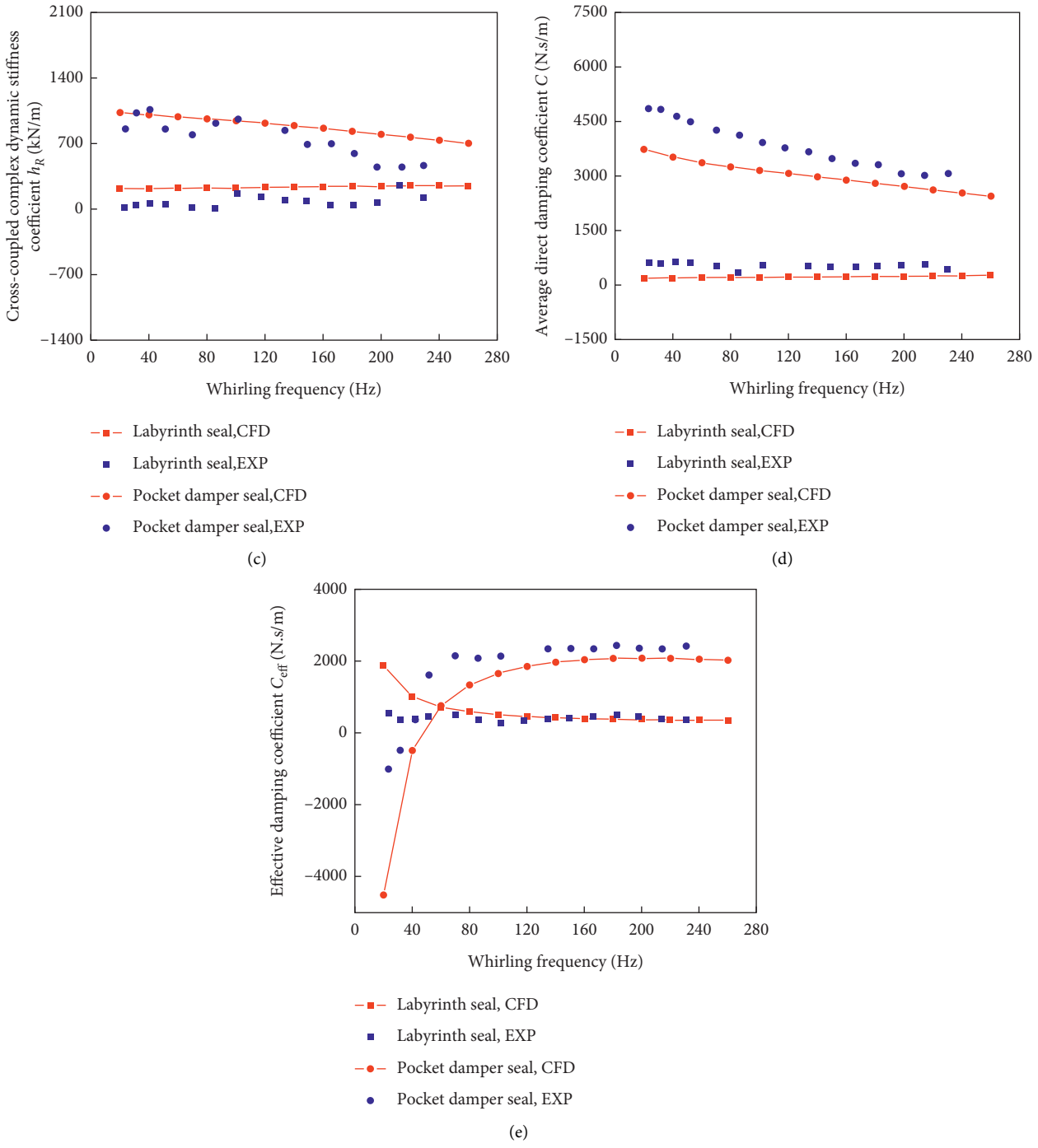

Figure 6: Comparison of experiments and current CFD results. (a) Leakage flow rate. (b) Direct complex dynamic stiffness coefficient. (c) Cross-coupled complex dynamic stiffness coefficient. (d) Average direct damping coefficient. (e) Effective damping coefficient.

Compared with the see-through labyrinth seal, the staggered labyrinth seal rotor has a convex plate structure, and the seal blades are different in height and staggered, which greatly increases the complexity of the flow field. It not only facilitates the formation of the whirling but also enhances the effect of the jet on the wall surface, which greatly increases the energy dissipation in the flow channel and reduces the leakage flow rate.

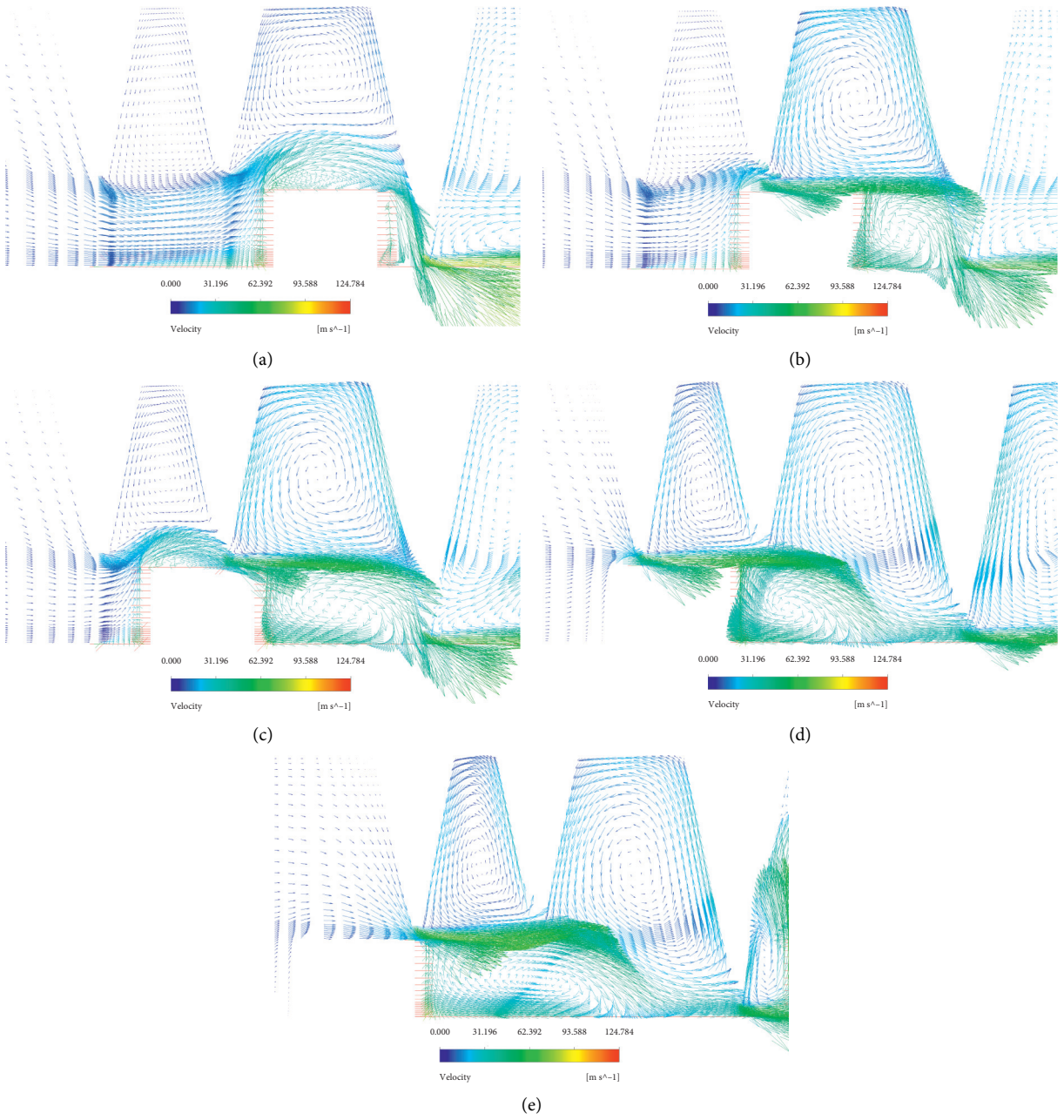

FIGURE 7: Velocity vector with a different rotor axial shifting. (a) z = -4 mm, (b) z = -2 mm, (c) z = 0 mm, (d) z = +2 mm, and (e) z = +5 mm.

To compare the leakage performance under different calculation conditions, the relative leakage rate r is defined as follows:

$$r = \frac{M_i - M_0}{M_0} \times 100\%, \tag{8}$$

where M_i (i = 1, 2, 3, ..., 14) is the calculated leakage flow rate under operating conditions and M_0 is the leakage flow rate of the original model.

Table 4 gives a comparison of the labyrinth seal leakage flow rate under various calculation conditions. The see-through labyrinth seal has a higher leakage flow rate of about 45.5% than the staggered labyrinth seal. The leakage flow rate of the staggered labyrinth seal for z = -2 mm is about 6% lower than that of the original model, and the leakage flow rate of the staggered labyrinth seal for b = 5.13 mm is about 5% lower than that of the original model. The leakage flow rate of staggered labyrinth seal decreases with the increasing height of rotor convex plate, the height of seal cavity, and the decrease in seal clearance.

3.2. Seal Dynamic Characteristic Analysis

3.2.1. Effect of the Rotor Axial Shifting Distances on the Dynamic Force Coefficients. Figures 8 and 9 display the variation of the direct complex dynamic stiffness coefficient

Table 4: Comparison of leakage flow rate under various calculation conditions.

Calculation conditions	Leakage flow rate (kg/s)	Relative leakage rate (%)
0	1.82859	/
1	2.2675	24.001
2	1.71819	-6.037
3	1.92639	5.348
4	2.08661	14.110
5	2.38674	30.524
6	2.62323	43.456
7	2.86433	56.641
8	1.8528	1.324
9	1.96453	7.434
10	1.73623	-5.051
11	1.86333	1.900
12	1.47783	-19.182
13	2.17809	19.113
14	2.66088	45.515

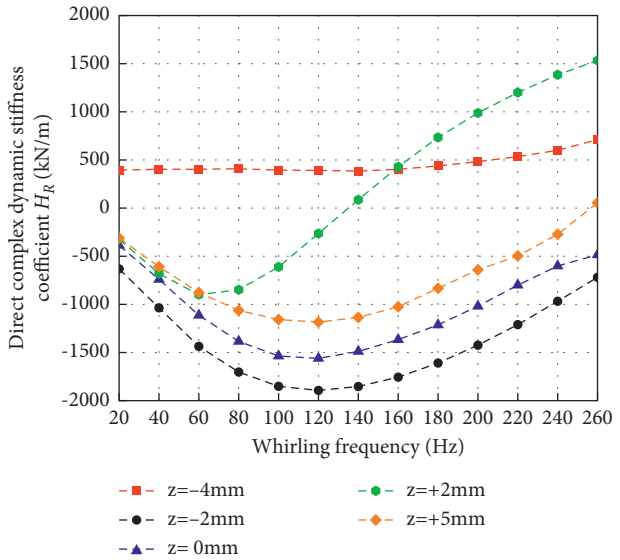

Figure 8: Direct complex dynamic stiffness coefficient vs. whirling frequency.

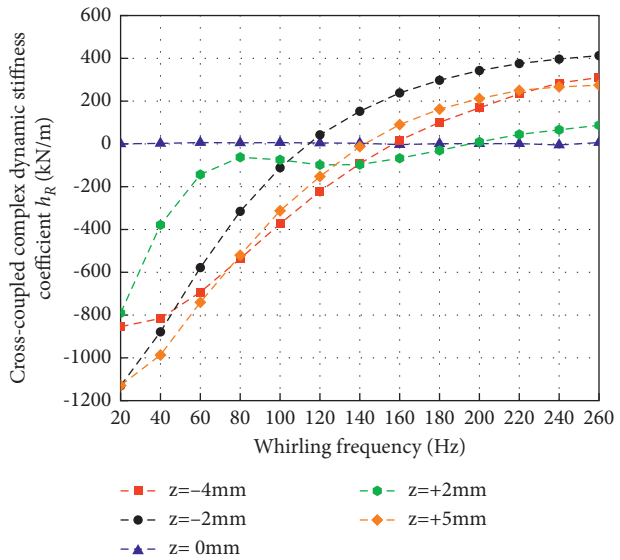

Figure 9: Cross-coupled complex dynamic stiffness coefficient vs. whirling frequency.

H_R and cross-coupled complex dynamic stiffness h_R with whirling frequency for different rotor axial shifting distances. For $z = -4$ mm, the direct complex dynamic stiffness coefficient H_R is relatively low in frequency dependence. For $z = +2$ mm, the H_R is relatively high in frequency dependence. For $z = 0$ mm, the cross-coupled complex dynamic stiffness coefficient h_R is close to zero. The h_R changes from negative to positive under shifting condition, and the frequency dependence is higher than that without shifting. For $z = -4$ mm, -2 mm, $+2$ mm, and $+5$ mm, the zero point of the h_R changes from negative to positive at the whirling frequency of approximately 160 Hz, 120 Hz, 200 Hz, and 140 Hz.

The average direct damping coefficient C_{avg} and the effective damping coefficient C_{eff} vary with whirling frequencies for various rotor axial shifting distances and are depicted in Figures 10 and Figure 11. The C_{avg} generally appears to increase with increasing whirling frequency, with minimal variation at rotor axial shifting of -4 mm. The C_{avg} of the rotor with positive axial shifting is relatively high. For $z = 0$ mm, the C_{eff} increases with the increasing whirling frequency. The cross-coupled complex dynamic stiffness coefficient h_R has little effect on the effective damping, and the average direct damping has a dominant influence on it. For $z \neq 0$ mm, the C_{eff} decreases with the increasing whirling frequency. For low whirling frequencies (<100 Hz), the effective damping is relatively high, and the stability of the rotor system is relatively strong. As the whirling frequency increases, the effective damping tends to be stable.

3.2.2. Effect of the Rotor Convex Plate Heights on the Dynamic Force Coefficients. Figures 12 and 13 depict the variation of the direct complex dynamic stiffness coefficient H_R and the cross-coupled complex dynamic stiffness coefficient h_R vs. whirling frequency for different rotor convex plate heights. For $a = 2.5$ mm, the direct complex dynamic stiffness

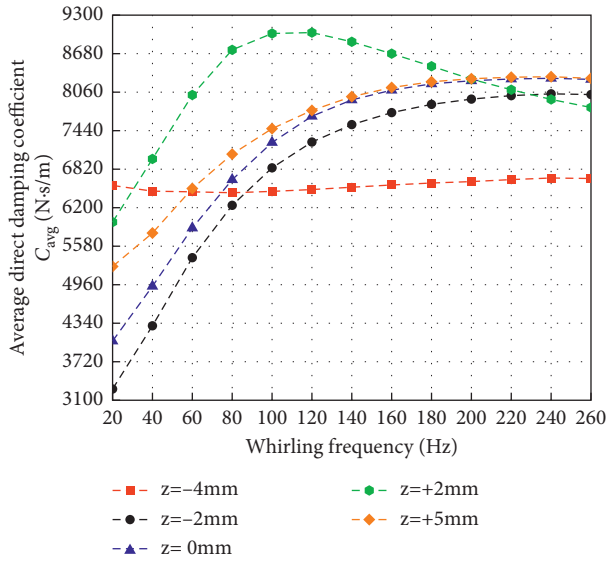

Figure 10: Average direct damping coefficient vs. whirling frequency.

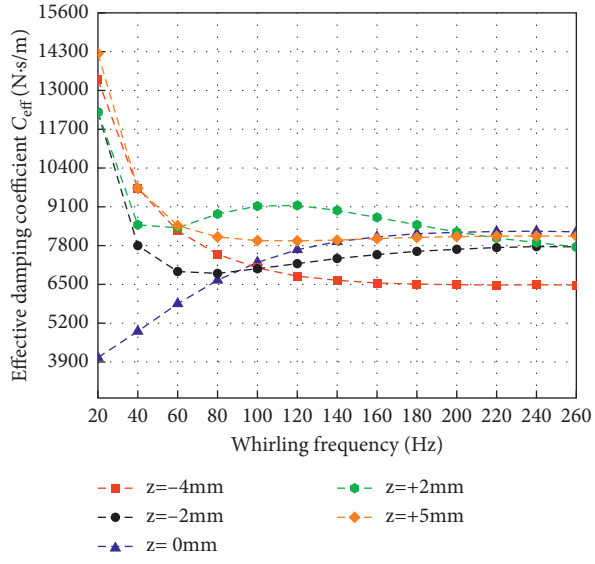

Figure 11: Effective damping coefficient vs. whirling frequency.

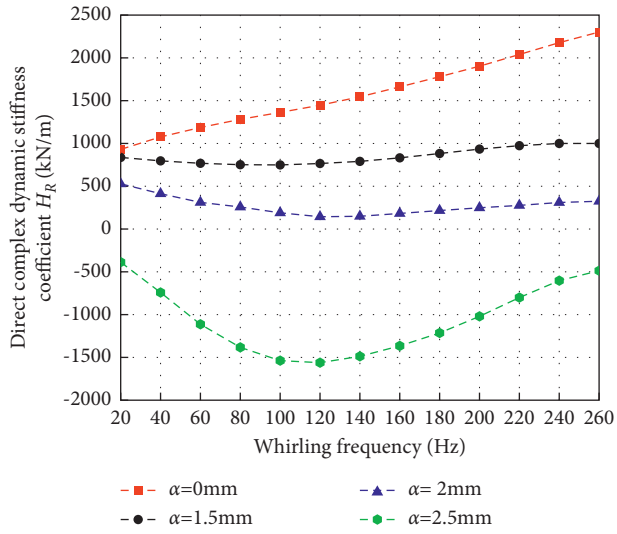

Figure 12: Direct complex dynamic stiffness coefficient vs. whirling frequency.

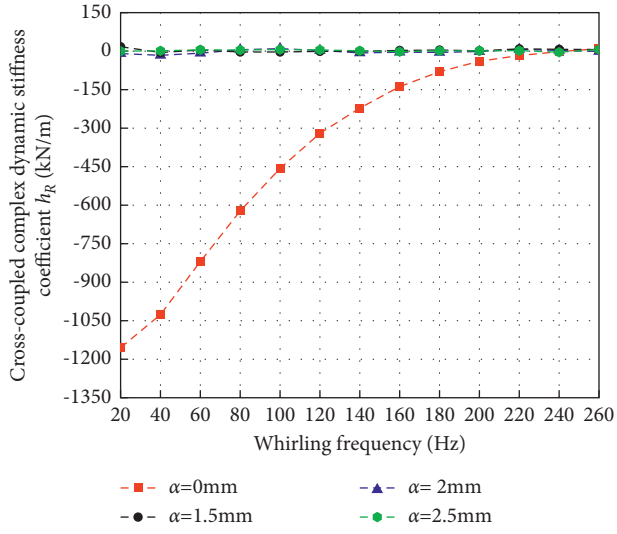

Figure 13: Cross-coupled complex dynamic stiffness coefficient vs. whirling frequency.

coefficient H_R is negative, and the rest are positive. With the increase in a, the direct complex dynamic stiffness coefficient increases. The cross-coupled complex dynamic stiffness coefficient h_R is negative for $a = 0$ mm, and its absolute value decreases with increasing whirling frequency, which has a strong frequency dependence. When $a \neq 0$ mm, the h_R is close to zero, showing frequency independence.

The average direct damping coefficient C_{avg} and the effective damping coefficient C_{eff} vary with whirling frequencies for various rotor convex plate heights and are depicted in Figures 14 and 15. For $a = 2.5$ mm, the C_{avg} frequency dependence is relatively strong. For $a = 0$ mm, the C_{avg} decreases with increasing whirling frequency, and it increases with increasing whirling frequency for $a = 2.0$ mm and 2.5 mm. When $a = 1.5$ mm, the C_{avg} has a relatively low amplitude with whirling frequency. When $a = 0$ mm, the h_R has a great influence on the effective damping coefficient C_{eff}. When $a \neq 0$ mm, the C_{avg} has a dominant influence on it. For $\Omega > 100$ Hz, the C_{eff} of $a = 2.5$ mm is higher than that of other different convex plate heights. When $a \neq 0$ mm, the C_{eff} increases with the increasing whirling frequency. When $a = 0$ mm, the C_{eff} decreases greatly with the increasing whirling frequency. For $\Omega > 160$ Hz, the C_{eff} of different convex plate heights tends to be stable. For $\Omega < 60$ Hz and $a \neq 0$ mm, the C_{eff} decreases with the increasing height of convex plate. For $\Omega > 60$ Hz and $a \neq 0$ mm, the C_{eff} increases with increasing height of rotor convex plate.

3.2.3. Effect of the Seal Cavity Heights on the Dynamic Force Coefficients. Figures 16 and 17 show the variation of the direct complex dynamic stiffness coefficient H_R and cross-

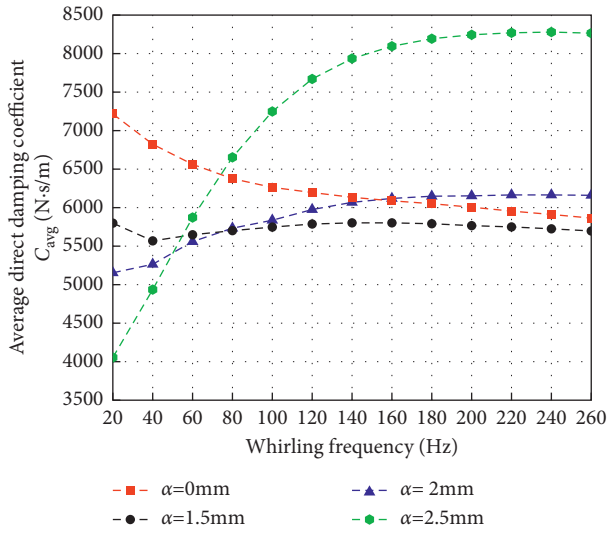

Figure 14: Average direct damping coefficient vs. whirling frequency.

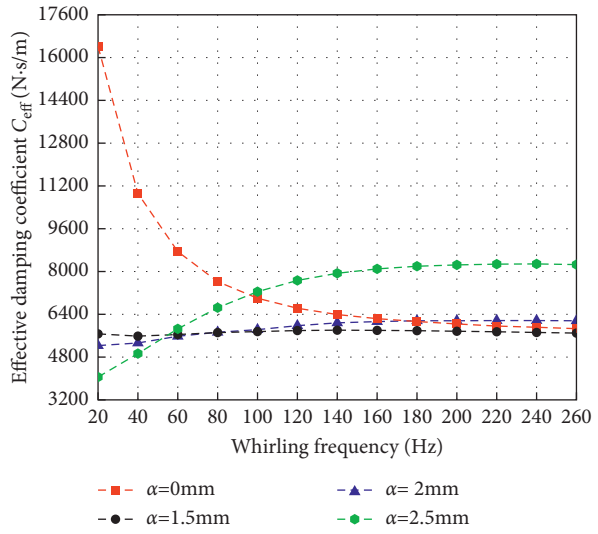

Figure 15: Effective damping coefficient vs. whirling frequency.

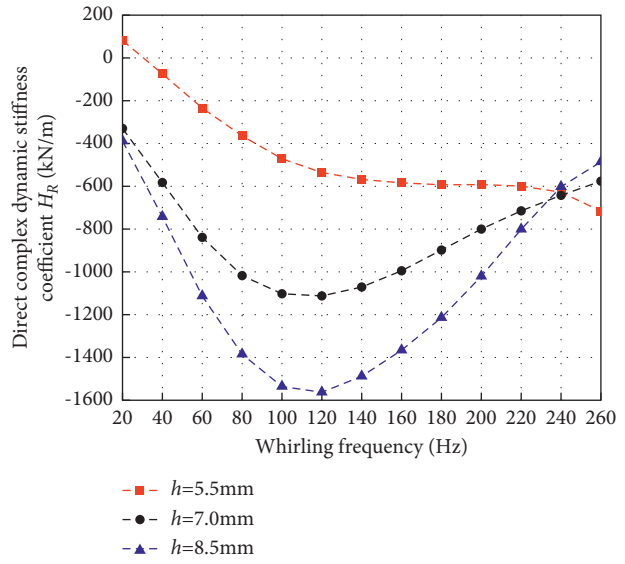

Figure 16: Direct complex dynamic stiffness coefficient vs. whirling frequency.

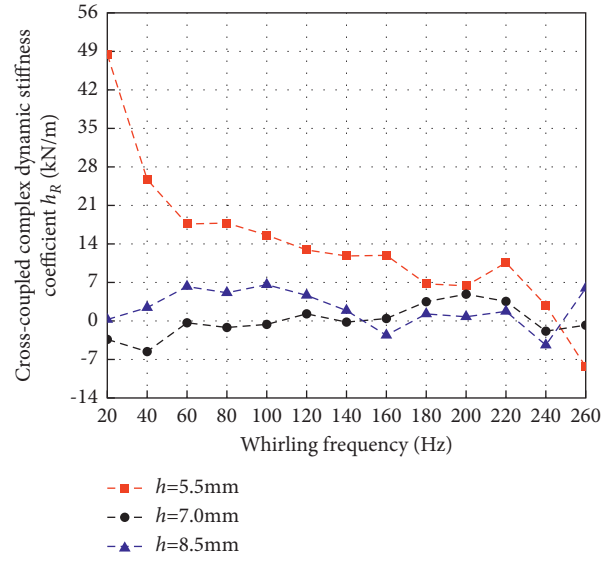

Figure 17: Cross-coupled complex dynamic stiffness coefficient vs. whirling frequency.

coupled complex dynamic stiffness coefficient h_R vs. whirling frequency for different heights of seal cavities. The H_R exhibits a quadratic nonlinear change with the whirling frequency increases. The absolute value of the H_R increases with the increasing height of the seal cavity when $\Omega < 240$ Hz, and the effect is opposite when $\Omega > 240$ Hz. As the whirling frequency increases, the direct complex dynamic stiffness coefficient first decreases and then increases. For $h = 5.5$ mm, the h_R decreases with the increasing whirling frequency, and it fluctuates around zero for $h = 7.0$ mm and 8.5 mm, and the frequency dependence is low.

Figures 18 and 19 depict the variation of the average direct damping coefficient C_{avg} and the effective damping coefficient C_{eff} vs. whirling frequency for different heights of seal cavities. The h_R has little effect on the C_{eff}, and the C_{avg} has a dominant influence on it. The C_{avg} and C_{eff} increase with the increasing whirling frequency, and the frequency dependence is strong. At low whirling frequencies ($\Omega < 140$ Hz), the damping coefficient generally increases with the decreasing height of the sealing cavity. At high whirling frequencies ($\Omega > 140$ Hz), the damping coefficient generally increases with the increasing height of the sealing cavity. As the whirling frequency increases, the stability of the rotor system is enhanced, which is conducive to the safe operation of the unit.

3.2.4. Effect of the Rotor Convex Plate Widths on the Dynamic Force Coefficients. The convex plate width was enlarged based on the original model. Figures 20 and 21 show the direct complex dynamic stiffness coefficient H_R and cross-

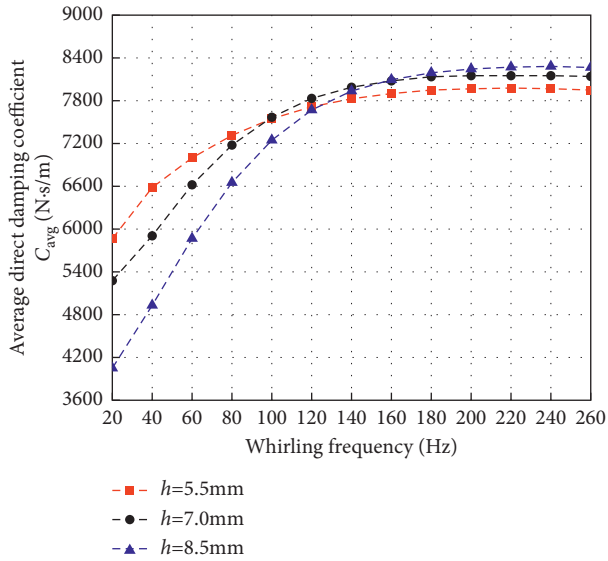

Figure 18: Average direct damping coefficient vs. whirling frequency.

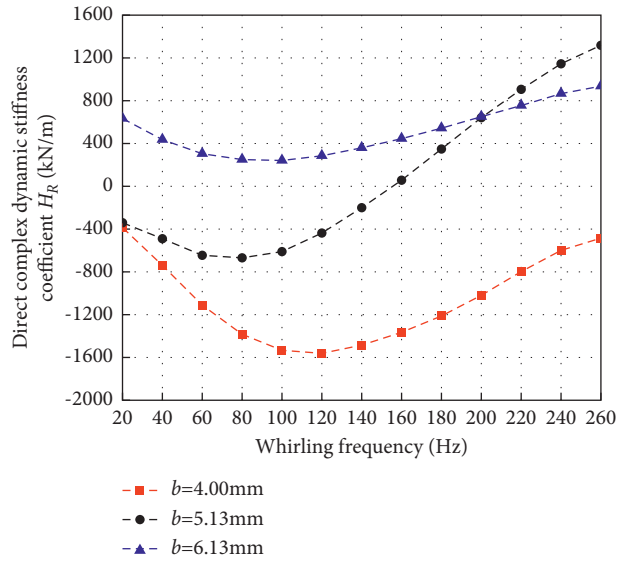

Figure 20: Direct complex dynamic stiffness coefficient vs. whirling frequency.

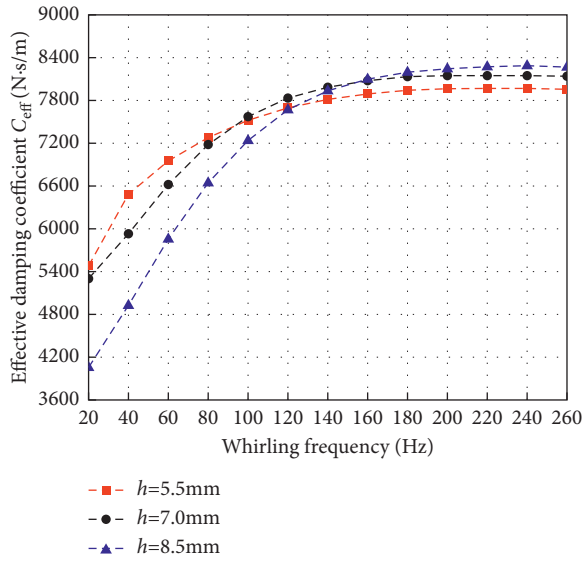

Figure 19: Effective damping coefficient vs. whirling frequency.

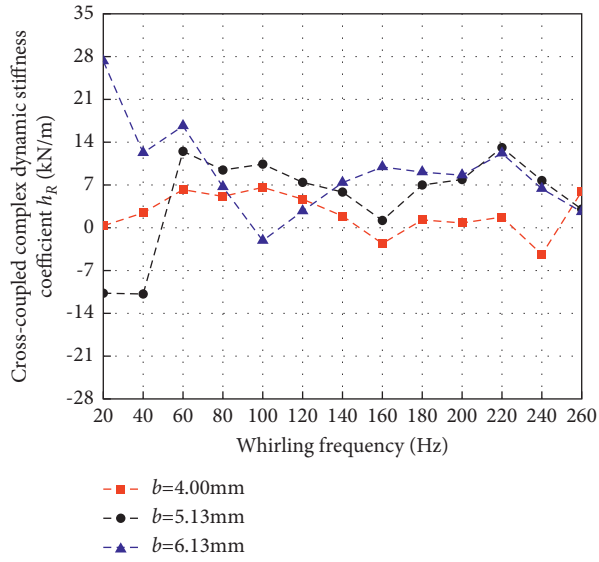

Figure 21: Cross-coupled complex dynamic stiffness coefficient vs. whirling frequency.

coupled complex dynamic stiffness coefficient h_R vs. whirling frequency for different widths of rotor convex plate. When $b = 6.13$ mm, 5.13 mm, and 4.00 mm, the H_R is positive, changes from negative to positive and negative, and exhibits quadratic nonlinear changes. For $\Omega < 200$ Hz, with the increase in b, the direct complex dynamic stiffness coefficient gradually decreases. Among them, $b = 6.13$ mm is less dependent on the whirling frequency. The h_R has low-frequency dependence and has little effect on the C_{eff}.

The average direct damping coefficient C_{avg} tends to be consistent with the C_{eff}, as shown in Figures 22 and 23. For $b = 4.00$ mm, the damping coefficient increases with the increasing whirling frequency. For $b = 5.13$ mm, the damping coefficient increases first and then decreases with the increasing whirling frequency. For $b = 6.13$ mm, the damping coefficient first increases with the whirling frequency and then becomes stable. The C_{eff} with $b = 5.13$ mm is relatively high, which is conducive to the stability of the sealing system. For $\Omega < 100$ Hz, the C_{eff} with $b = 6.13$ mm is higher than 4.00 mm. Otherwise, the C_{eff} with $b = 4.00$ mm is higher than that with 6.13 mm.

3.2.5. Effect of Sealing Clearances on the Dynamic Force Coefficients. Figures 24 and 25 depict the direct complex dynamic stiffness coefficient H_R and cross-coupled complex dynamic stiffness coefficient h_R vs. whirling frequency for different sealing clearances. The H_R exhibits a quadratic

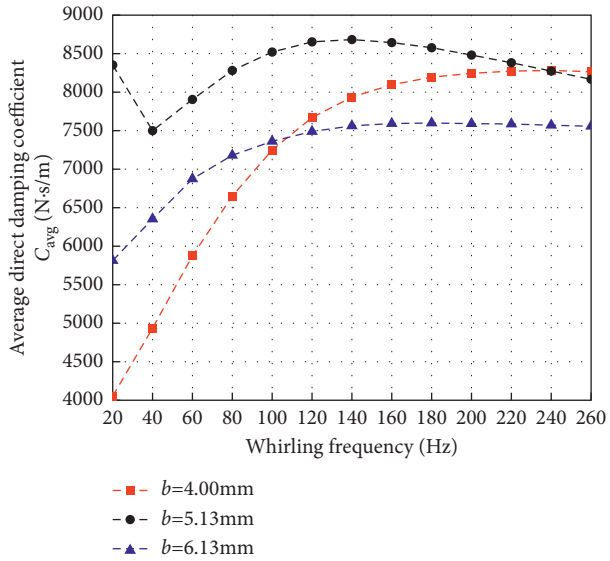

Figure 22: Average direct damping coefficient vs. whirling frequency.

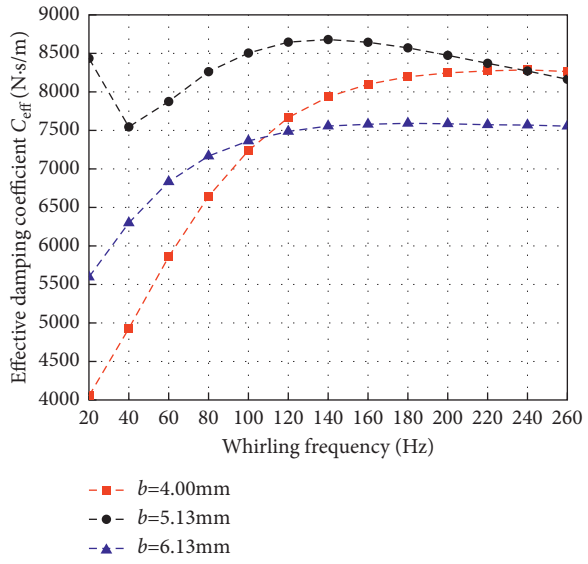

Figure 23: Effective damping coefficient vs. whirling frequency.

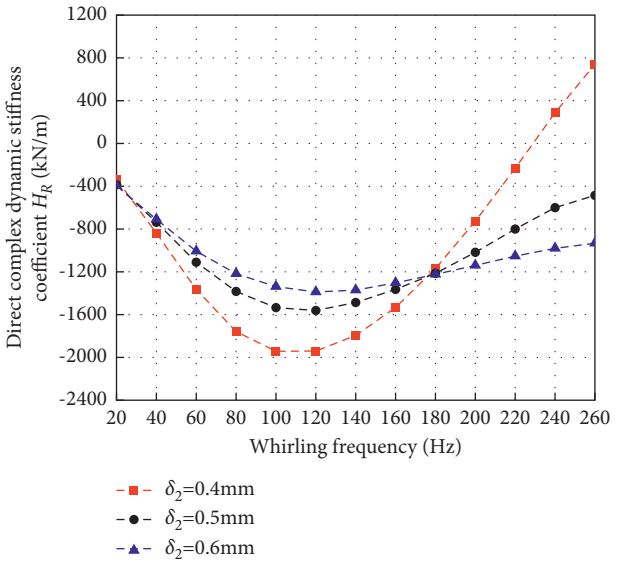

Figure 24: Direct complex dynamic stiffness coefficient vs. whirling frequency.

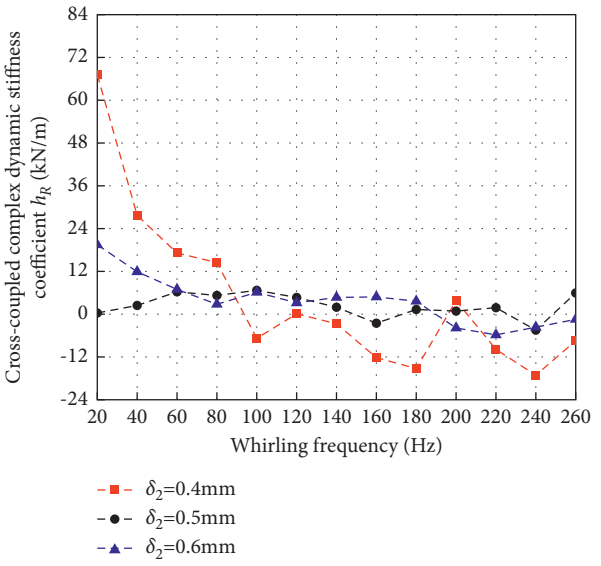

Figure 25: Cross-coupled complex dynamic stiffness coefficient vs. whirling frequency.

nonlinear change with the whirling frequency increases. The absolute value of the H_R decreases with the increasing sealing clearance when $\Omega < 180$ Hz, and the effect is opposite when $\Omega > 180$ Hz, great frequency dependence on whirling frequency, and the system stability is high at high frequencies. The h_R of $\delta_2 = 0.4$ mm is changed from positive to negative. When $\delta_2 = 0.5$ mm and $\delta_2 = 0.6$ mm, the h_R changes stably with the whirling frequency, and the frequency dependence is low.

As shown in Figures 26 and 27, the h_R has little effect on the effective damping C_{eff}, and the C_{avg} has a dominant influence on it. The C_{eff} increases with the increasing whirling frequency and the decreasing sealing clearance. When the sealing clearance is 0.4 mm, the C_{eff} is about 116%–148% of that with the clearance of 0.6 mm, and the frequency dependence decreases with the increasing seal clearance.

3.2.6. Effect of the Sealing Type on the Dynamic Force Coefficients. Figures 28 and 29 depict the direct complex dynamic stiffness coefficient H_R and cross-coupled complex dynamic stiffness coefficient h_R vs. whirling frequency for different seal structures. The H_R of the see-through labyrinth seal is negative, the H_R of the staggered labyrinth seal is positive, and the see-through labyrinth seal frequency dependence is relatively strong. The h_R of the staggered labyrinth seals tends to zero, and the h_R of the see-through labyrinth seal is negative, and its absolute value decreases with increasing whirling frequency, and the frequency dependence is relatively high.

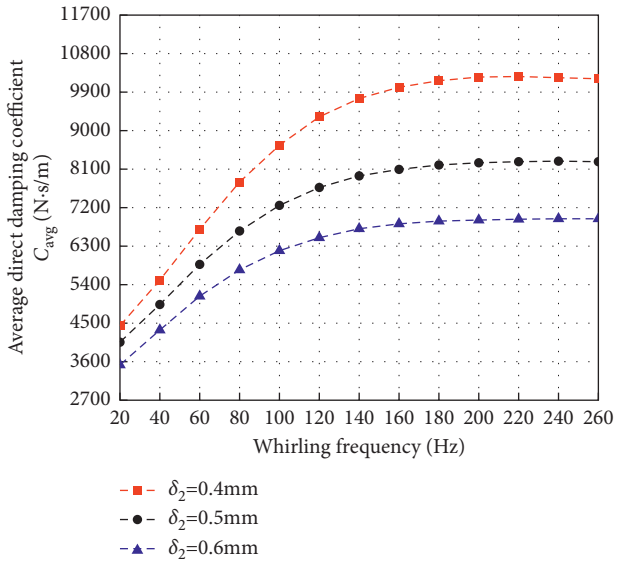

FIGURE 26: Average direct damping coefficient vs. whirling frequency.

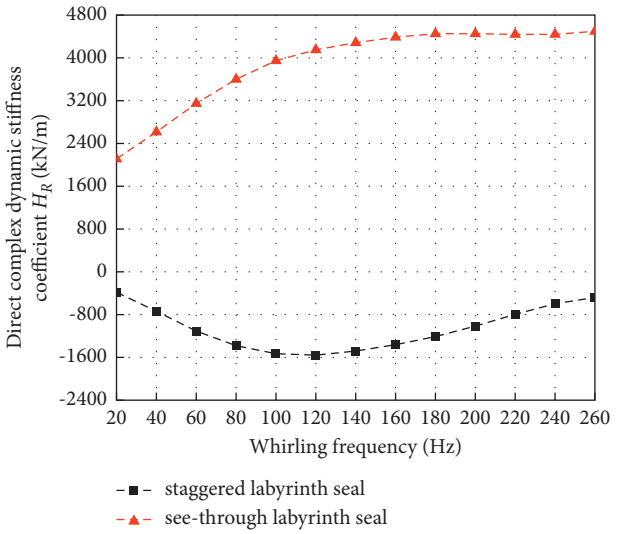

FIGURE 28: Direct complex dynamic stiffness coefficient vs. whirling frequency.

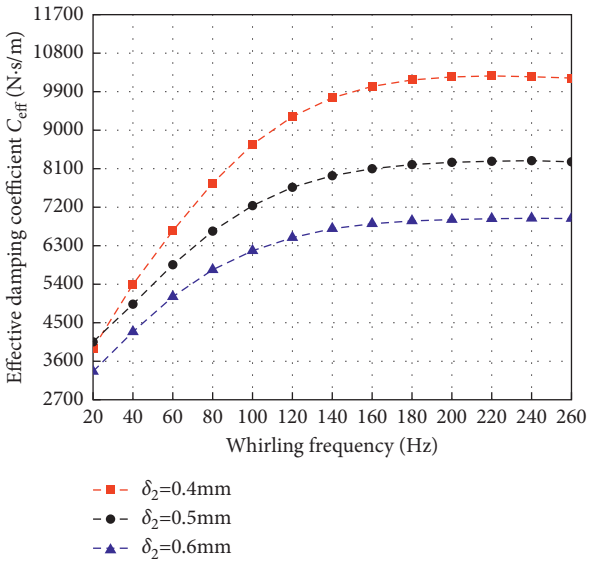

FIGURE 27: Effective damping coefficient vs. whirling frequency.

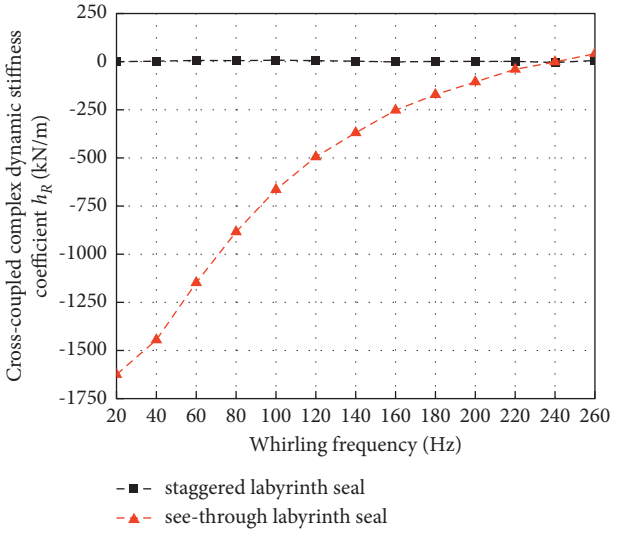

FIGURE 29: Cross-coupled complex dynamic stiffness coefficient vs. whirling frequency.

The variations of average direct damping coefficient C_{avg} and effective damping coefficient C_{eff} vs. whirling frequencies for different seal structures are depicted in Figures 30 and 31, respectively. The C_{avg} and C_{eff} of the see-through labyrinth seals decrease with the increasing whirling frequency, while the C_{avg} and C_{eff} of the staggered labyrinth seal increase with the increasing whirling frequency. For $\Omega < 160$ Hz, the C_{eff} of the see-through labyrinth seal is significantly higher than that of the staggered labyrinth seal, which is about 107%–649% of the staggered labyrinth seal. Otherwise, the C_{eff} of the staggered labyrinth seal is about 105%–113% of the see-through labyrinth seal. The sealing system possesses better stability.

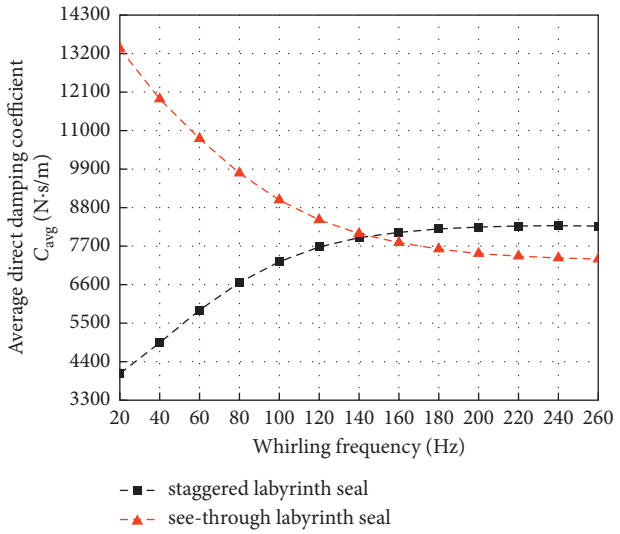

FIGURE 30: Average direct damping coefficient vs. whirling frequency.

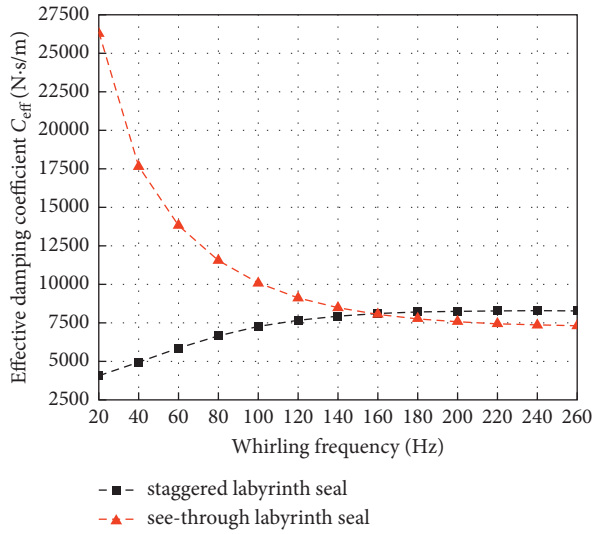

FIGURE 31: Effective damping coefficient vs. whirling frequency.

4. Conclusions

This study reports a comprehensive investigation on the leakage and rotordynamic performance of the staggered labyrinth seal working with supercritical carbon dioxide. A computational fluid dynamic method is employed to establish a fully three-dimensional numerical model for the staggered labyrinth seal. An identification method based on the infinitesimal theory is applied to obtain the dynamic force coefficients. The CFD model predicts the dynamic force coefficients for the seals operating under various rotor axial shifting distances, heights/widths of rotor convex plate, heights of seal cavity, and sealing clearance conditions. Several conclusions are summarized as follows.

The C_{eff} of the seal with positive axial shifting is higher than that with negative shifting, and the sealing system is more stable. When the rotor with convex plate operates without axial shifting, the h_R of the staggered labyrinth seal has low-frequency dependence and has little effect on the C_{eff}. The C_{avg} has a dominant influence on the C_{eff}.

For $\Omega < 60$ Hz and $a \neq 0$ mm, the C_{eff} decreases with the increasing height of convex plate. For $\Omega > 60$ Hz and $a \neq 0$ mm, the C_{eff} increases with increasing height of rotor convex plate. For $\Omega < 140$ Hz, the damping coefficient generally increases with the decreasing seal cavity height. Otherwise, the damping coefficient generally increases with increasing seal cavity height. For $\Omega < 160$ Hz, the C_{eff} of the see-through labyrinth seal is about 107%–649% of the staggered labyrinth seal. For $\Omega > 160$ Hz, the C_{eff} of the staggered labyrinth seal is about 105%–113% of the see-through labyrinth seal. The C_{eff} for the seal with the rotor convex plate width of 5.13 mm is relatively high, which is conducive to the stability of the sealing system. The C_{eff} increases with the decreasing seal clearance. The C_{eff} of 0.4 mm clearance is about 116%–148% of 0.6 mm.

The see-through labyrinth seal has a higher leakage flow rate of about 45.5% than the staggered labyrinth seal. The rotor axial shifting is -2 mm, and the width of rotor convex is 5.13 mm, which is about 6% and 5% lower than that of the original model. The leakage flow rate of the staggered labyrinth seal decreases with the increasing height of rotor convex plate, the seal cavity height, and the decreasing seal clearance.

Nomenclature

m, n:	Amplitudes of excitation (mm)
C_{avg}:	Average direct damping coefficient (N·s/m)
C_{eff}:	Effective damping coefficient (N·s/m)
H_R, h_R:	Direct and cross-coupled complex dynamic stiffness coefficient (kN/m)
C_{xx}, C_{yy}, C_{xy}, C_{yx}:	Direct and cross-coupled damping coefficient (N·s/m)
R:	Seal inner radius (mm)
h:	Cavity depth (mm)
h_1:	Low blade height (mm)
h_2:	High blade height (mm)
d_1:	Low blade root length (mm)
d_2:	High blade root length (mm)
d:	Blade thickness (mm)
l_1:	Low blade 1 and low blade 2 distance (mm)
l_2:	Low blade 2 and high blade distance (mm)
l_3:	High blade and low blade 1 distance (mm)
δ_1:	Low blade and rotor clearance distance (low blade and convex plate clearance distance) (mm)
δ_2:	High blade and rotor clearance distance (mm)
a:	Convex plate height (mm)
z:	Rotor axial shifting distance (mm)
b:	Convex plate width (mm)
K_{xx}, K_{yy}, K_{xy}, K_{yx}:	Direct and cross-coupled stiffness coefficient (kN/m)
M_{xx}, M_{yy}, M_{xy}, M_{yx}:	Direct and cross-coupled inertial coefficient (kg)
P_{in}:	Supply pressure (MPa)

P_{out}: Discharge pressure (MPa)
T: Temperature (K)
ω: Rotational speed of the rotor (RPM)
Ω: Whirling frequency (Hz)
r: Relative leakage rate (%)
M_i: Leakage flow rate under operating conditions (kg/s)
M_0: Leakage flow rate of the original model (kg/s).

Data Availability

All data included in this study are available upon request to the corresponding author.

Conflicts of Interest

The authors declare that they have no conflicts of interest.

Acknowledgments

The authors are grateful for the grants from the National Natural Science Foundation of China (51875361).

References

[1] G. Angelino, "Carbon dioxide condensation cycles for power production," *Journal of Engineering for Power*, vol. 90, no. 3, pp. 287–295, 1968.

[2] E. G. Feher, "The supercritical thermodynamic power cycle," *Energy Conversion*, vol. 8, no. 2, pp. 85–90, 1968.

[3] O. V. Combs, *An Investigation of the Supercritical CO2 Cycle (Feher Cycle) for Shipboard Application*, Massachusetts Institute of Technology, Cambridge, MA, USA, 1977.

[4] Y. Ahn, S. J. Bae, M. Kim et al., "Review of supercritical CO2 power cycle technology and current status of research and development," *Nuclear Engineering and Technology*, vol. 47, no. 6, pp. 647–661, 2015.

[5] S. A. Wright, P. S. Pickard, R. Fuller, R. F. Radel, and M. E. Vernon, "Supercritical CO2 Brayton cycle power generation development program and initial test results," in *Proceedings of the ASME 2009 Power Conference*, pp. 573–583, Albuquerque, MX, USA, January 2009.

[6] K. J. Kimball, K. D. Rahner, J. P. Nehrbauer, and E. M. Clementoni, "Supercritical carbon dioxide Brayton cycle development overview," in *Proceedings of the ASME Turbo Expo 2013: Turbine Technical Conference and Exposition*, San Antonio, TX, USA, June, 2013.

[7] E. M. Clementoni, T. L. Cox, and C. P. Sprague, "Startup and operation of a supercritical carbon dioxide Brayton cycle," in *Proceedings of the ASME Turbo Expo 2013: Turbine Technical Conference and Exposition*, San Antonio, TX, USA, June 2013.

[8] S. D. Cich, J. J. Moore, M. Marshall, K. Hoopes, J. Mortzheim, and D. Hofer, "Radial inlet and exit design for a 10 MWe SCO2 axial turbine," in *Proceedings of the ASME Turbo Expo 2019: Turbomachinery Technical Conference and Exposition*, Phoenix, AZ, USA, June, 2019.

[9] S. D. Cich, J. J. Moore, M. D. Towler, J. Mortzheim, and D. Hofer, "Loop filling and start up with a closed loop SCO2 Brayton cycle," in *Proceedings of the ASME Turbo Expo 2019: Turbomachinery Technical Conference and Exposition*, Phoenix, AZ, USA, June, 2019.

[10] J. Moore, K. Brun, N. Evans, and C. Kalra, "Development of 1 MWe supercritical CO2 test loop," in *Proceedings of the ASME Turbo Expo 2015: Turbine Technical Conference and Exposition*, Montréal, Canada, June, 2015.

[11] M. Utamura, H. Hasuike, K. Ogawa et al., "Demonstration of Supercritical CO2 Closed Regenerative Brayton Cycle in a Bench Scale Experiment," in *Proceedings of the ASME Turbo Expo 2012: Turbine Technical Conference and Exposition*, Copenhagen, Denmark, June, 2012.

[12] J. Lee, J. I. Lee, Y. Ahn, and H. Yoon, "Design Methodology of Supercritical CO2 Brayton Cycle Turbomachineries," in *Proceedings of the ASME Turbo Expo 2012: Turbine Technical Conference and Exposition*, Copenhagen, Denmark, June, 2012.

[13] Y. Ahn, J. Lee, S. G. Kim, and J. I. Lee, "Studies of supercritical carbon dioxide Brayton cycle performance coupled to various heat sources," in *Proceedings of the ASME 2013 Power Conference*, Boston, MA, USA, July, 2013.

[14] J. Schmitt, R. Willis, D. Amos, J. Kapat, and C. Custer, "Study of a supercritical CO2 turbine with TIT of 1350 K for Brayton cycle with 100 MW class output: aerodynamic analysis of stage 1 vane," in *Proceedings of the ASME Turbo Expo 2014: Turbine Technical Conference and Exposition*, Düsseldorf, Germany, June, 2014.

[15] D. Zhang, Y. Wang, and Y. Xie, "A SCO2 turbine device adaptive to wide-range mass flow rate and backpressure," vol. 6, 2017.

[16] F. Behafarid and M. Z. Podowski, "Modeling and computer simulation of centrifugal CO2 compressors at supercritical pressures," *Journal of Fluids Engineering*, vol. 138, no. 6, Article ID 061106, 2016.

[17] T. W. Kim, N. H. Kim, and K. Y. Suh, "Computational fluid dynamics analysis for an optimal supercritical carbon dioxide turbine blade," *Transactions of the American Nuclear Society*, vol. 95, pp. 790-791, 2006.

[18] T. W. Kim, W. S. Jeong, and K. Y. Suh, "Numerical modeling and analysis of supercritical carbon dioxide turbine," *Transactions of the American Nuclear Society*, vol. 98, pp. 499–450, 2008.

[19] M. Odabaee, E. Sauret, and K. Hooman, "CFD simulation of a supercritical carbon dioxide radial-inflow turbine, comparing the results of using real gas equation of estate and real gas property file," *Applied Mechanics and Materials*, vol. 846, pp. 85–90, 2016.

[20] J. Wang, Y. Huang, Y. Zan, and X. Lang, *A Turbo-Generator with SCO2 as a Working Fluid*, CN, Ontario, Canada, 2016.

[21] H. Tian, Y. Ma, M. Li, S. Liu, and K. Wang, "Leakage research on supercritical carbon dioxide fluid in rolling piston expander," *Science China Technological Sciences*, vol. 55, no. 6, pp. 1711–1718, 2012.

[22] S. R. Pidaparti, *A Computational Study on the Leakage of Supercritical Carbon Dioxide through Labyrinth Seals*, Texas A&M University, College Station, TX, USA, 2013.

[23] H. Yuan, S. Pidaparti, M. Wolf, J. Edlebeck, and M. Anderson, "Numerical modeling of supercritical carbon dioxide flow in see-through labyrinth seals," *Nuclear Engineering and Design*, vol. 293, pp. 436–446, 2015.

[24] J. A. Bennett, W. Paudel, A. F. Clarens, B. Weaver, and C. Watson, "Computational analysis of seals for sCO2 turbomachinery and experimental planning," in *Proceedings of the The 6th International Supercritical CO2 Power Cycles Symposium*, Pittsburgh, PA, USA, March, 2018.

[25] Y. Zhu, Y. Jiang, S. Liang, Y. Guo, C. Guo, and P. Yue, "Numerical study of super-critical carbon dioxide flow in

stepped-staggered labyrinth seals," in *Proceedings of the The 6th International Supercritical CO2 Power Cycles Symposium*, Pittsburgh, PA, USA, March, 2018.

[26] Z. Li, F. Zhi, F. Li, J. Li, and Z. Feng, *Design and Research of 450 MWe Supercritical Carbon Dioxide Turbine Shaft Sealing Scheme*, China Society of Engineering Thermophysics, Xi an, China, 2018.

[27] Q. Du, K. Gao, D. Zhang, and Y. Xie, "Effects of grooved ring rotation and working fluid on the performance of dry gas seal," *International Journal of Heat and Mass Transfer*, vol. 126, pp. 1323–1332, 2018.

[28] W. Shen, X. Peng, and J. Jiang, "Analysis on real effect of supercritical carbon dioxide dry gas seal at high speed," *Ciesc Journal*, vol. 70, no. 7, pp. 2645–2659, 2019.

[29] W. Zhang, Q. Gu, J. Yang, and C. Li, "Application of a novel rotordynamic identification method for annular seals with arbitrary elliptical orbits and eccentricities," *ASME Journal of Engineering for Gas Turbines and Power*, vol. 141, no. 9, Article ID 091016, 2019.

[30] ANSYS, *CFX-Solver Theory Guide. Release 11.0*, ANSYS, Canonsburg, PA, USA, 2006.

[31] R. Span and W. Wagner, "A new equation of state for carbon dioxide covering the fluid region from the triple-point temperature to 1100 K at pressures up to 800 MPa," *Journal of Physical and Chemical Reference Data*, vol. 25, no. 6, pp. 1509–1596, 1996.

[32] H. Yuan, S. Pidaparti, M. Wolf, and M. Anderson, "Experiment and Numerical Study of Supercritical Carbon Dioxide Flow through Labyrinth Seals," in *Proceedings of the The 4th International Symposium - Supercritical CO2 Power Cycles*, Pittsburgh, PA, USA, September, 2014.

[33] B. Ertas and J. Vance, "The influence of same-sign cross-coupled stiffness on rotordynamics," *Journal of Vibration and Acoustics*, vol. 129, no. 1, pp. 24–31, 2007.